

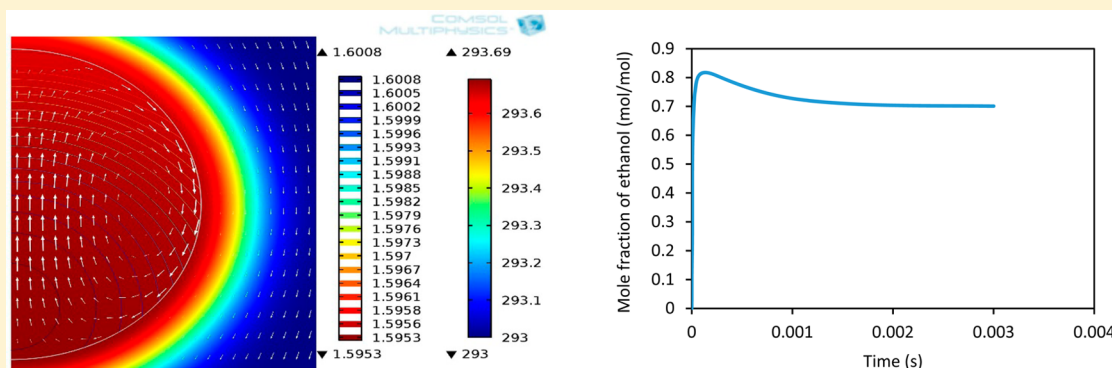
Purification of Bioethanol Using Microbubbles Generated by Fluidic Oscillation: A Dynamical Evaporation Model

Nada N. Abdulrazzaq,^{†,‡} Baseem H. Al-Sabbagh,^{†,‡} Julia M. Rees,^{*,§} and William B. Zimmerman[†]

[†]Department of Chemical and Biological Engineering, University of Sheffield, Mappin Street, Sheffield, S1 3JD, U.K.

[‡]Department of Chemical Engineering, College of Engineering, University of Baghdad, Baghdad, Iraq

[§]School of Mathematics and Statistics, University of Sheffield, Hounsfield Road, Sheffield, S3 7RH, U.K.



ABSTRACT: A computational model of a single gas microbubble immersed in a liquid of ethanol–water mixture is developed and solved numerically. This complements earlier binary distillation experiments in which the ethanol–water mixture is stripped by hot air microbubbles achieving around 98% vol. ethanol from the azeotropic mixture. The proposed model has been developed using Galerkin finite element methods to predict the temperature and vapor content of the gas microbubble as a function of its residence time in the liquid phase. This model incorporates a novel rate law that evolves on a time scale related to the internal mixing of microbubbles of 10^{-5} s. The model predictions of a single bubble were shown to be in very good agreement with the existing experimental data, demonstrating that the ratio of ethanol to water in the microbubble regime are higher than the expected ratios that would be consistent with equilibrium theory for all initial bubble temperatures and all liquid ethanol mole fractions considered and within the very short contact times appropriate for thin liquid layers. Our previous experiments showed a decrease in the liquid temperature with decreasing liquid depth in the bubble tank, an increase in the outlet gas temperature with decreasing liquid depth, and an improvement in the stripping efficiency of ethanol upon decreasing the depth of the liquid mixture and increasing the temperature of the air microbubbles, all of which are consistent with the predictions of the computational model.

1. INTRODUCTION

The progressive depletion of fossil-based fuels coupled with the negative effects caused by their emissions on the environment, has motivated the search for renewable sources of energy. Since bioethanol can be derived from renewable materials such as biomass and is associated with low carbon emissions, it is considered as one of the most viable alternative fuels to gasoline.¹ Over the years, many technologies for separating ethanol–water mixtures have been proposed and tested.² Most of them, however, are associated with high energy requirements and operational difficulties.³ Industrially, distillation is the main technology considered for ethanol purification.^{4,5} However, the formation of constantly boiling mixtures (i.e., an azeotrope) limits the degree of purity for numerous chemicals.^{3,6} This issue can be overcome by adding a third component to break the azeotrope. This requires more steps for separating the additional chemicals and consequently more energy is needed.⁷

The separation of liquid mixtures by bringing the liquid phase into contact with a gas phase is a major technique for separating solutions into their original constituents. Direct contact evaporation (DCE) has been widely used for many years for concentrating and separating aqueous solutions through injecting fine (1–3 mm)⁸ to coarse (~1 cm)⁹ superheated gas bubbles. Bubbles are normally created by injecting a gas phase into a turbulent flow through a porous material, perforated plate, or a set of perforated pipes located at the bottom of a bubble column or evaporator containing the target solution. Owing to the absence of any separating walls between the processing fluids, this technique has myriad applications in industrial processes that involve gas–liquid

Received: April 29, 2016

Revised: October 28, 2016

Accepted: November 28, 2016

Published: November 28, 2016

systems.¹⁰ High thermal efficiency, which reaches to around 95% with a temperature difference of only 2–5 °C between the bubble and the liquid phases, is the main feature that characterizes this process from conventional ones.^{11–16}

If the gas phase is injected as a cloud of uniformly dispersed, noncoalescent microbubbles, (as shown in Figure 1),^{17–19} there

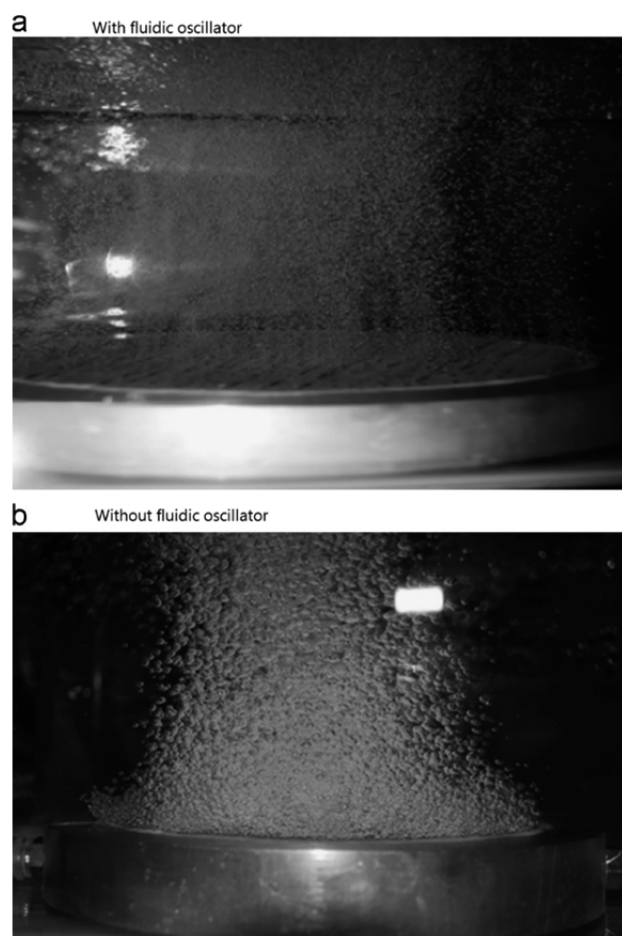


Figure 1. Images of microbubble generation using a microporous ceramic diffuser under different conditions (a) with fluidic oscillator and (b) without fluidic oscillator.²²

exists a potential for increasing the rates of both heat and mass transfers. The high surface area to volume ratio offered by microbubbles will enhance the heat and mass transfers since the rates of these interfacial transport processes are hugely dependent on the contact area between the gas and liquid phases. Additionally, smaller bubbles have high internal pressures due to surface tension which also significantly enhances the driving force for both heat and mass transfers.^{20,21}

When hot bubbles are injected into a cold liquid they transfer their energy to the surrounding mixture in two ways: either as latent heat of evaporation, resulting in an evaporation of the liquid mixture from the surface to the interior of the bubble, or as a sensible heat transfer, causing a rise in the temperature of the liquid mixture. It used to be assumed that the energy transmitted by the bubbles is split evenly between heat and mass transfer largely due to liquid turbulent mixing.⁹ However, recent experiments in this field based on pure water have shown that upon decreasing the residence time of microbubbles in a liquid mixture, evaporation begins to dominate over heat transfer, while at longer residence times, heat transfer

dominates and the initially evaporated liquid is recondensed and returns from the bubble to the surrounding mixture.²² The recondensation process is associated with a release of sensible heat to the liquid mixture which leads to an increase in its temperature. The residence time of bubbles in the liquid mixture can be simply controlled by altering the depth of the liquid layer through which the bubbles can ascend. This means that when the depth of the liquid layer is shallow, evaporation becomes favorable which leads in turn to a maximum separation efficiency. As the depth of the liquid layer increases, sensible heat transfer becomes more significant leading to a reduction in vaporization as well as raising the temperature of the liquid mixture.²²

Following these findings, we have conducted experiments on the separation of an ethanol–water binary liquid mixture with superheated air microbubbles generated by a fluidic oscillator such as those shown in Figure 1^{17,23–25} using a laboratory scale rig (see ref 26 for the details of the experimental procedure and the equipment used). It was demonstrated how the application of a thin film of liquid, through which the bubbles can ascend, can shift the separation process far from the equilibrium state. It was also found that the efficiency of the removal of ethanol from the liquid mixture can be increased effectively by reducing the depth of the liquid in the bubble tank. Furthermore, the enrichment of ethanol in the vapor phase at thin liquid layers is higher than that achieved at equilibrium conditions for different microbubble inlet temperatures and different liquid ethanol compositions, including the azeotrope.²⁶

The work reported here aims to establish a numerical model using the technique of computational fluid dynamics (CFD) to describe the dynamics of superheated microbubbles, generated by fluidic oscillation, in the binary distillation of ethanol–water mixtures and validate it with the earlier experimental evidence.²⁶ The key element of this model is that microbubble internal mixing occurs on a time scale of $\sim 10^{-3}$ s,²² so an evaporating mixture or condensing vapor must obey a rate law that evolves on this rapid time scale. No such rate law has been previously used, so it is introduced here originally. The study also aims to explore the effect of important parameters such as bubble size, initial bubble temperature, and liquid composition on the efficiency of the stripping process. These predictions are of primary importance not only for the robust design of the system but also for the optimization of the process operating parameters.

This paper is organized as follows: section 2 presents the governing equations for the computational model with their initial and boundary conditions as well as the numerical methods for solving the equations. A sensitivity study to investigate the effect of the main parameters governing the process is presented in section 3, while in section 4 conclusions of this study are drawn.

2. MODEL DEFINITION

The system investigated comprises a single fluidic oscillator air microbubble, such as in Figure 1, of a diameter 200 μm (dispersed phase) which rises due to a buoyancy force in an infinite reservoir of ethanol–water mixture. The width of the liquid domain is taken to be 10 times that of the bubble radius. Simulation domains of 6–10 bubble radius widths have shown that the walls have little effect on the bubble shape and velocity field.²⁷

The simulation study of this system incorporates a time dependent model for the temperature and concentration

profiles inside the bubble. Circulation patterns due to bubble motion are also set up inside and around the bubble. To simplify the system, the model adopted here is based on the following assumptions: (1) The bubble has spherical shape. This is because the bubble is sufficiently small that its surface tension is quite strong so there is no deformation from the spherical shape. This assumption is a good approximation for the micro-sized bubble used in this study. (2) The bubble is always rising at its terminal velocity. This simplifies the calculations through focusing only on the mass and heat transfer dynamics. (3) The pressure inside the bubble is constant which is reasonable for the rather small residence times applied in this study. (4) The concentration profile in the liquid phase is constant. The continuous phase is completely mixed with a constant bulk concentration. This assumption is reasonable so attention can be restricted to solving the transfer equations only inside the bubble instead of solving them both inside and outside. (5) No chemical reaction occurs in either phase. The physical parameters used in the computational model are given in Table 1.

Table 1. Physical Properties for the Evaporation Dynamics of a Hot Bubble Rising in an Ethanol–Water Mixture (Ethanol (1) and Water (2))

quantity	value
liquid mixture density	$\exp(x_1 \times \ln \rho_1 + x_2 \times \ln \rho_2 - 30.808[(x_1 x_2)/T_{\text{liquid}}] - 18.274[(x_1 x_2(x_2 - x_1))/T_{\text{liquid}}] + 13.8[(x_1 x_2)(x_2 - x_1)^2/T_{\text{liquid}}]) \text{ kg/m}^3$
ethanol density (ρ_1)	$0.791 \times 10^3 \text{ kg/m}^3$
water density (ρ_2)	$1 \times 10^3 \text{ kg/m}^3$
liquid mixture viscosity	$\exp(x_1 \times \ln \mu_1 + x_2 \times \ln \mu_2 + 724.652[(x_1 x_2)/T_{\text{liquid}}] + 729.357[(x_1 x_2)(x_2 - x_1)/T_{\text{liquid}}] + 976.05[(x_1 x_2)(x_2 - x_1)^2/T_{\text{liquid}}]) \text{ Pa s}$
ethanol viscosity (μ_1)	$1.1890 \times 10^{-3} \text{ Pa s}$
water viscosity (μ_2)	$1.003 \times 10^{-3} \text{ Pa s}$
C_p water (liquid)	75.33 J/mol/K
C_p ethanol (liquid)	110.5 J/mol/K
C_p water (vapor)	$33.46 + 0.688 \times 10^{-2}(T - 273) + 0.7604 \times 10^{-5}(T - 273)^2 - 3.593 \times 10^{-9}(T - 273)^3 \text{ J/mol/K}$
C_p ethanol (vapor)	$61.34 + 15.72 \times 10^{-2}(T - 273) - 8.749 \times 10^{-5}(T - 273)^2 + 19.83 \times 10^{-9}(T - 273)^3 \text{ J/mol/K}$
C_p air	$28.09 + 0.1965 \times 10^{-2}T + 0.4799 \times 10^{-5}T^2 - 1.965 \times 10^{-9}T^3 \text{ J/mol/K}$
P^* water	$133.322368 \exp(18.3036 - (3816.44/(-46.13 + T))) \text{ Pa}$
P^* ethanol	$133.322368 \exp(18.5242 - (3578.91/(-50.50 + T))) \text{ Pa}$
K air	$(0.007058 + 0.0000578T + 1.9751 \times 10^{-8}T^2) \text{ W/m/K}$
ΔH_v water	$56462.6 - 43.1784T + 0.000962433T^2 + 3.5155 \times 10^{-6}T^3 - 8.9825 \times 10^{-10}T^4 \text{ J/mol}$
ΔH_v ethanol	$1048.6 - 1.0921(T - 273) + 0.010651(T - 273)^2 - 0.00020693(T - 273)^3 + 1.1231 \times 10^{-6}(T - 273)^4 - 2.4928 \times 10^{-9}(T - 273)^5 \text{ J/kg}$

2.1. Governing Equations. In this system, heat and mass transfers occur simultaneously leading to heating and vaporization of the liquid. The time dependent temperature and concentration profiles of the microbubble can be obtained from the simultaneous solution of the energy and mass transfer equations inside the bubble. Considering the simplifications previously mentioned, the following equations for mass and heat transfers are the main governing equations for this model:

$$\frac{\partial c_i}{\partial t} + u \cdot \nabla c_i = D \nabla^2 c_i \quad (1)$$

$$\frac{\partial T}{\partial t} + u \cdot \nabla T = \alpha \nabla^2 T \quad (2)$$

where c_i is the molar concentration of ethanol ($i = e$) and water ($i = w$) in the bubble, T is the temperature of the bubble field, D is molecular diffusivity, u is the velocity inside the bubble and α is the thermal diffusivity of the air. Gas properties (thermal conductivity, heat capacity, and thermal diffusivity) are considered to be temperature dependent and calculated according to polynomial empirical correlations.²⁸ Gas density and gas molecular diffusivities are taken as constant. Liquid mixture properties (density, viscosity, and thermal conductivity) were calculated according to the concentration-dependent correlations.²⁹

The internal velocity field of the bubble is calculated by Hill's spherical vortex³⁰ which is the solution of the Navier–Stokes equation adopted by Hadamard and Rybcynski for small spherical bubbles rising under a buoyancy force.³¹ The stream function for this flow is given by

$$\psi = \frac{1}{2} U_t R^2 \left(\frac{r}{R} \right)^2 \left[1 - \left(\frac{z}{R} \right)^2 - \left(\frac{r}{R} \right)^2 \right] \quad (3)$$

from which the dimensionless axial (z) and radial (r) velocity components are derived:

$$u_r = -\frac{1}{r} \frac{\partial \psi}{\partial z} \quad (4)$$

$$u_z = \frac{1}{r} \frac{\partial \psi}{\partial r} \quad (5)$$

The velocities are computed to be

$$u_z = U_t \left(1 - \left(\frac{z}{R} \right)^2 - 2 \left(\frac{r}{R} \right)^2 \right) \quad (6)$$

$$u_r = U_t \frac{r}{R} \frac{z}{R} \quad (7)$$

$$U_t = \frac{1}{3} \frac{g R^2}{\mu} \Delta \rho \quad (8)$$

where u_z and u_r are the velocity vectors in axial and radial coordinates respectively, R is the radius of the bubble, U_t is the terminal velocity for a bubble rising under gravitational acceleration g , μ is the viscosity of the surrounding liquid and $\Delta \rho$ is the density difference.

The velocity field outside the bubble (in the liquid domain) is calculated from the dimensionless Stokes stream function equation for a uniform far-field flow:³²

$$\psi = -\frac{1}{2} U_t r^2 \left[1 - \frac{3}{2} \frac{R}{\sqrt{r^2 + z^2}} + \frac{1}{2} \left(\frac{R}{\sqrt{r^2 + z^2}} \right)^3 \right] \quad (9)$$

from which the dimensionless radial (r) and axial (z) velocity components are calculated according to the formulas given by eqs 4 and 5.

2.2. Initial and Boundary Conditions. Equations 1 and 2 must be solved with suitable initial and boundary conditions. Microbubbles containing bone dry air are injected initially at temperature T_0 (the initial concentrations for water and ethanol

are zero). For the liquid domain, the initial temperature is 293 K for all calculations.

Boundary conditions were introduced for both heat and mass transfers. The temperature at the side walls of the computational domain is fixed at 293 K. At the gas–liquid interface, the common assumption for calculating the composition of species is that there is liquid–vapor equilibrium.^{22,33–36} Fixing the surface concentration of the transport species to their saturation values, however, cannot be justified for the current system since it is working far from equilibrium conditions.²⁶ In this case, a kinetic model for the evaporation rate can be adopted, for instance, Langmuir law for evaporation from thin films, to calculate the mass flux for each component at the interface:

$$\dot{n}_i = k_i A (x_i \gamma_i P_i^* - P_i) \quad (10)$$

where \dot{n}_i is the evaporation rate for each species at the interface, A is the gas–liquid contact area, k_i is the evaporation constant which represents the amount of component evaporated per unit time per unit area per unit pressure, x_i is the mole fraction, γ_i is the activity coefficient, P_i^* is the saturation vapor pressure at the gas–liquid interface, and P_i is the partial pressure of the vapor at the bubble bulk (i.e., inside the bubble) for each component. For the case of heat transfer, the boundary condition is

$$\hat{n} \cdot K \nabla T = \sum \dot{n}_i \Delta H_{vi} \quad (11)$$

The normal heat flux at the interface was calculated using Fourier's law which is equated to the latent heat of vaporization ΔH_{vi} weighted by the evaporation rate \dot{n}_i at the interface for each component. \hat{n} is the normal vector and K is the thermal conductivity.

Equation 10 simplifies to Raoult's Law modified with the activity coefficient at equilibrium conditions, that is, $\dot{n}_i = 0$, thereby stating that evaporation (or condensation) is driven by the difference of the interfacial partial pressure from its predicted Raoult's Law value at equilibrium. Partial pressures of vapor components in the bubble P_i were calculated using the ideal gas law because of the conditions of low pressures and high temperatures considered here. The activity coefficients were calculated using the Wilson model²⁸ at the bubble interface temperature, while vapor pressures P_i^* were calculated using the Antoine eq 28. The evaporation parameter for water (k_w) is difficult to predict. Himus and Hinchley³⁷ measured this parameter experimentally for pure water evaporated by air and found it to be around 5×10^{-6} mol/m² Pa·s. For our system, this unknown parameter was estimated using a least-squares error method and our experimental data on the separation of ethanol–water mixtures²⁶ with the value found by Himus and Hinchley³⁷ as an initial guess. The minimum error was associated with a value of 2.4×10^{-5} mol/m² Pa·s for water (k_w). For ethanol (k_e), the best approximation was found to be 2.5 times greater than that of water, in accord with the ratio of their vapor pressures.

2.3. Numerical Method. Numerical simulations were carried out using the Galerkin finite element method (FEM) with COMSOL Multiphysics V4.3a in order to solve the governing equations. Simulations were carried out on two computers. The first one contained an Intel Core i5-2430 M CPU running at 2.4 GHz with 6 GB of installed memory and the second one had 12 processors and 96 GB of installed memory; 56 620 triangular mesh elements were used to create

the domain of the computational model. Because of the axisymmetry, calculations were carried out in a semicircle in the r – z plane.

The numerical stability of the results was checked by varying the mesh refinement while monitoring the change in the average mole fraction of ethanol and the nondimensional bubble temperature ratio (T_b/T_0) after 0.002 s. Mesh comparisons are presented in Table 2. The average mole

Table 2. Grid Convergence Results at $t = 0.002$ s

grid	no. of elements	ethanol [%mol]	T_b/T_0
1	56620	0.70460	0.74728
2	68236	0.70461	0.74727
3	86422	0.70463	0.74726
4	100790	0.70464	0.74726

fraction of ethanol and the temperature ratio differed by only 0.0057% and 0.0027%, respectively, between grid meshes containing 56 620 and 100 790 elements. For this reason, grid (1) was adopted for the further calculations as it has the least computational cost.

3. SIMULATION RESULTS AND DISCUSSION

The results of the numerical simulations for the circulating microbubble are presented in this section. The initial focus will be on discussing the trends of the temperature and concentration profiles of the microbubble with time. Then, a sensitivity study of the effect of varying bubble size, initial bubble temperature, liquid composition, and the parameter k_w on the simulation results, will be presented in the subsequent section.

3.1. Simulation Profiles. The microbubble profile of ethanol concentration distribution, temperature field and velocity vectors is shown in Figure 2 after 0.0015 s.

Clearly, the temperature profile is nearly isothermal at 294 K and the concentration profile of ethanol is nearly constant

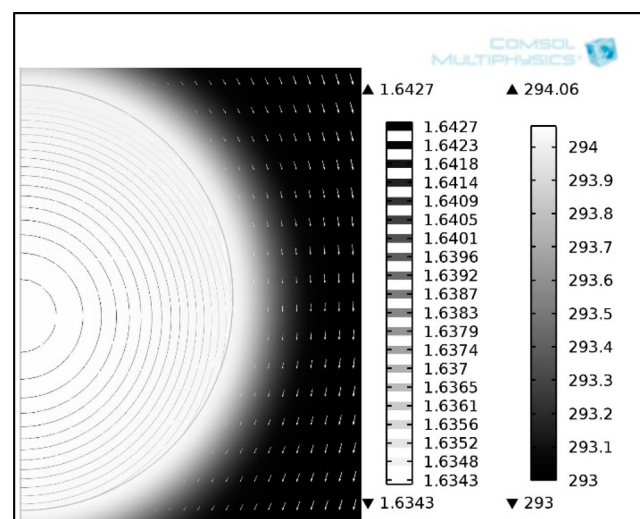


Figure 2. Microbubble profile with $R = 100 \mu\text{m}$, $T_0 = 423$ K, ambient liquid temperature of 293 K, and 50% mole initial ethanol liquid concentration after $t = 0.0015$ s. The arrows represent the steady state velocity field inside and outside the bubble. The contours indicate ethanol concentration (mol/m³) inside the bubble and the shading represents the temperature (K).

throughout the bubble at around 1.64 mol/m^3 . This outcome is mainly due to the intensive internal circulation of the microbubble which helps to homogenize it both thermally and chemically at sufficiently early residence times in the liquid.^{22,38,39}

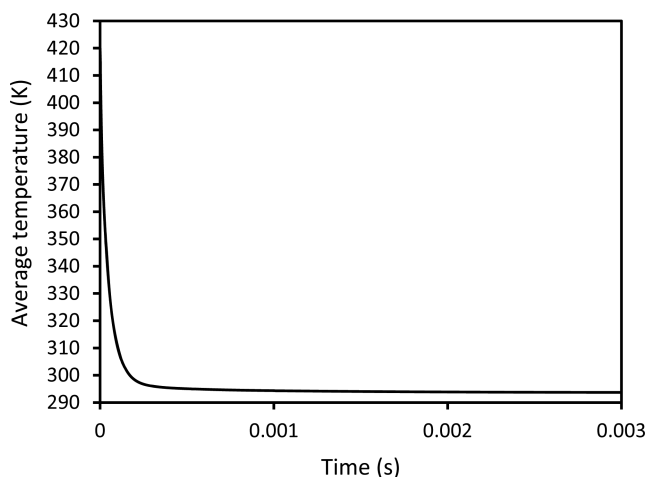


Figure 3. Variation of the average microbubble temperature with time. The initial conditions are 50% mole ethanol liquid concentration and bone dry air with $T_0 = 423 \text{ K}$ injected in the microbubbles.

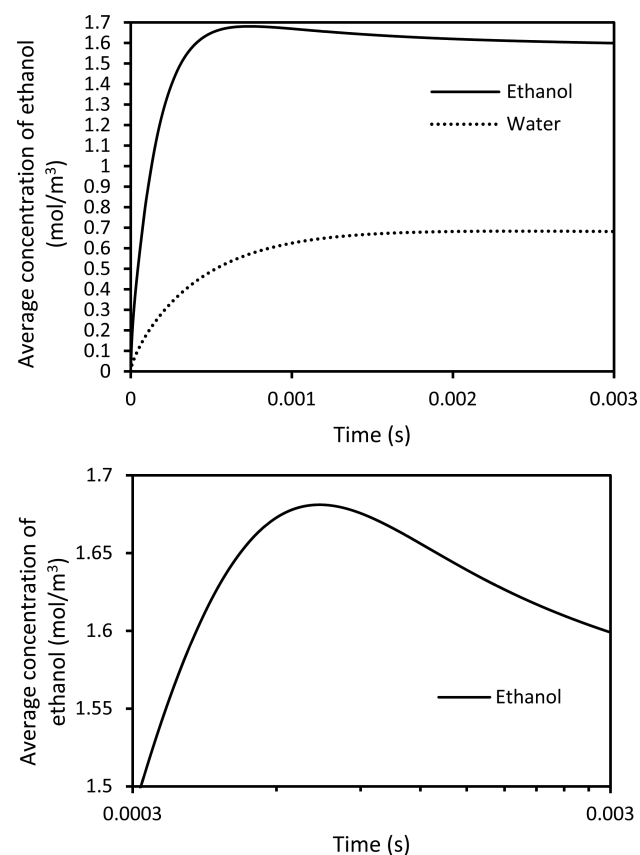


Figure 4. Variation of the average concentration of ethanol and water in the microbubble with time. The initial conditions are 50% mole ethanol liquid concentration and bone dry air with $T_0 = 423 \text{ K}$ injected in the microbubbles.

Figures 3, 4, and 5 show respectively the time profiles for the average bubble temperature, the average bubble concentration and the average mole fraction obtained from the numerical simulations.

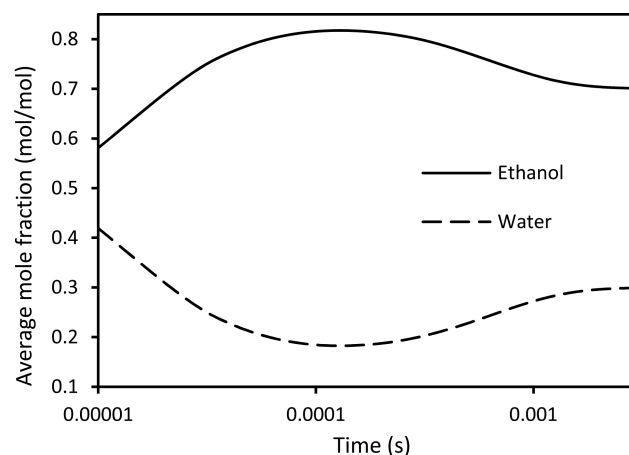


Figure 5. Variation of the average mole fractions of ethanol and water in the microbubble with time (i.e., the air is ignored). The initial conditions are 50% mole ethanol liquid concentration and bone dry air with $T_0 = 423 \text{ K}$ injected in the microbubbles.

Simulation profiles indicate that the heat and mass transfer dynamics of the microbubble are strongly time-dependent. Figure 3 shows that the average temperature profile decreases rapidly with time from its initial value of 423 K until it almost reaches equilibrium with the ambient temperature of 293 K after 0.003 s . This behavior can be attributed to the effect of liquid evaporation into the bubble. When vaporization occurs, latent heat of evaporation is lost which causes the bubble temperature to decrease sharply at short contact times.

Figure 4 shows the change of the average composition of ethanol inside the circulating microbubble with the residence time in the liquid phase. This figure clarifies how the maximum ethanol concentration is rapidly attained within a very short contact time (around 0.00072 s) in the liquid due to the high internal convection in the microbubble²² which leads to a fast evolution of the vapor concentration. Beyond this point (i.e., 0.00072 s), condensation of the previously evaporated vapors occurs as the bubble cools, causing a decrease in the concentration of vapor in the bubble and sensible heat transfer to the liquid. This means that there is competition between the latent and sensible heat transfers and the dominance of either of them depends on the residence time of the microbubble in the liquid phase. At shorter bubble residence times, a greater level of evaporation can be achieved; however, at longer contact times, sensible heat becomes more important. It is possible to control the contact time of the rising microbubbles in the liquid so that the transfer processes (i.e., evaporation and heat transfer) can be preferentially selected for transfer to or from the microbubble. Contact times for the microbubbles can be set experimentally by altering the depth of the liquid through which bubbles can rise. If the application requires high heat transfer efficiency, higher liquid depths are used to maximize sensible heat transfer. However, for applications for which temperature rise is not favorable, such as those dealing with thermally sensitive materials, shallower liquid levels should be applied to reduce the residence times of the bubbles and to achieve more evaporation. These results are consistent with the

findings of Abdulrazzaq et al.²⁶ for the evaporation of the ethanol–water binary system which showed that the concentration of ethanol in the vapor phase increased as the height of liquid mixture layer decreased.

Figure 5 presents the time profiles of the mole fractions of both ethanol and water within the core of the bubble which shows that the maximum ratio for ethanol to water was achieved at 1.3×10^{-4} s and decreased thereafter. The reason for this outcome is that the chance of ethanol evaporation is higher initially because of its higher vapor pressure than that of water. However, as time passes, the concentration difference of ethanol across the film at the gas–liquid interface drops, leading to an increase in the likelihood of water vaporization. Figure 6 presents information about the change of the

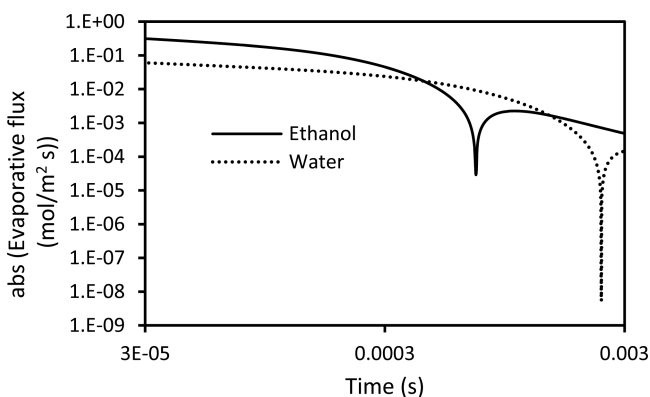


Figure 6. A log–log plot for the average mass fluxes for ethanol and water at the bubble skin versus time. The results show that the interfacial fluxes for ethanol and water switch from evaporation to condensation at 7.2×10^{-4} s and 2.4×10^{-3} s, respectively. The initial conditions are 50% mole ethanol liquid concentration and bone dry air with $T_0 = 423$ K injected into the microbubbles.

evaporation rate at the bubble skin with time. As can be seen, the evaporation rates for both ethanol and water are higher initially and then drop to negative values (i.e., the condensation effect).

3.2. Variation of Bubble Size. The most critical parameter that affects the interfacial mass and heat transfers across the gas–liquid interface is bubble size. Figure 7 shows the effect of different bubble sizes on the average concentration of ethanol

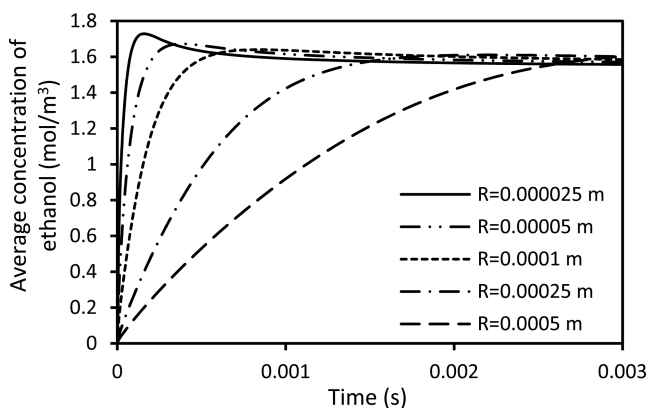


Figure 7. Variation of the average concentration of ethanol with bubble size. The initial bubble temperature is $T_0 = 393$ K and the initial liquid concentration is 50% mole ethanol.

obtained from seven model computations. Liquid concentration and initial temperature of the bubble were kept at 50% mole and 393 K for all calculations.

Numerically, these results demonstrate that small bubbles are more efficient in the stripping of ethanol than larger bubbles especially at very short residence times in the liquid. In comparison with fine bubbles, microbubbles have higher surface area to volume ratios, higher residence times and more intensive internal velocity rates.²² These properties lead to a faster evolution of the vapor concentration inside the microbubble and thereby render them more effective than fine bubbles in the separation process at shorter contact times. As time passes, the concentration of microbubbles approaches that of the larger bubbles. This occurs because microbubbles lose most of their contents when they cool due to the condensation effect. Figure 8 shows clearly how tiny bubbles

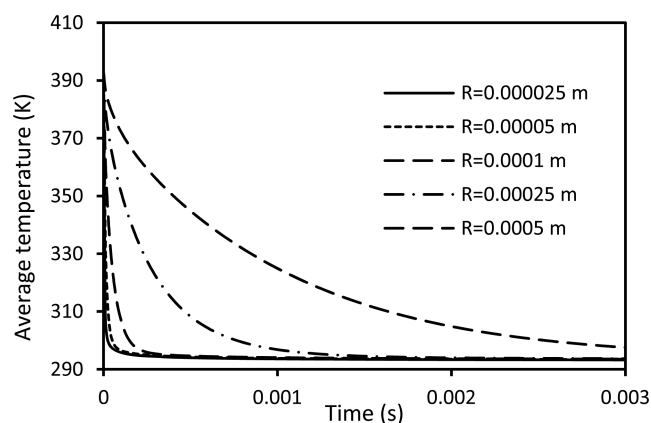


Figure 8. Variation of the average temperature of the bubble with bubble size: $R = 0.0005$ m (top), $R = 0.00025$ m, $R = 0.0001$ m, $R = 0.00005$ m, $R = 0.000025$ m (bottom). Initial bubble temperature is $T_0 = 393$ K and initial liquid concentration is 50% mole ethanol.

can deliver most of their provided enthalpy at sufficiently shorter residence times in the liquid phase while larger bubbles are almost still at their initial injection temperature because of their weak internal convection.²²

These findings are in agreement with the results of an analogous mass transfer only study that was conducted by Ubal et al.³⁸ on a single buoyant rising liquid drop. In their model, a study of the effect of the internal circulation of a drop on the mass transfer dynamics confirmed that the evolution of mass transfer for a circulating drop is much faster than that of a rigid one (i.e., without circulation) in which the mass profile is confined within a thin layer near the drop skin.

3.3. Variation of Inlet Gas Temperature. Figure 9 presents the comparison of five average ethanol concentration profiles at various inlet microbubble temperatures. The liquid temperature and initial liquid mole fraction were kept at 293 K and 50% mole respectively for all simulations.

The results show that the maximum concentration of ethanol rises with the inlet microbubble temperature and that the lower the initial bubble temperature is, the slower is the recondensation progressed.

Increasing the bubble temperature causes an increase in the vapor pressures of the components in the liquid mixture, thereby increasing the fraction of evaporated components into the bubble phase. This is in agreement with our previous results obtained from the separation of the ethanol–water system by

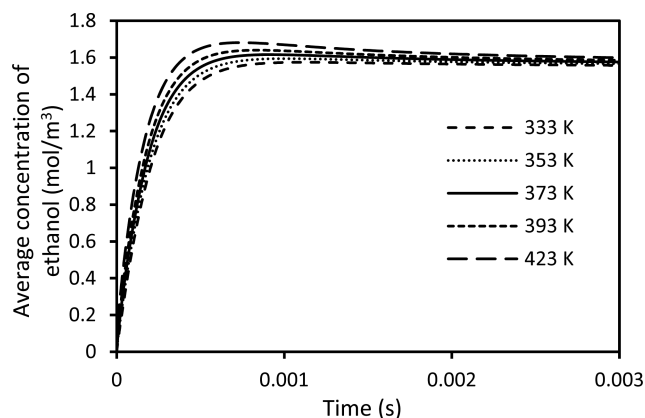


Figure 9. Variation of the average concentration of ethanol with bubble temperatures $T_0 = 423$ K (top line), 393, 373, 353, and 333 K (bottom line). The initial condition is bone dry air injected into the microbubbles.

microbubbles which demonstrated an improvement in the separation efficiency of ethanol with increasing bubble temperature.²⁶

At longer residence times, all bubbles reached thermal equilibrium with the surrounding liquid mixture as shown in Figure 10 at a temperature of 293 K and concentration of about

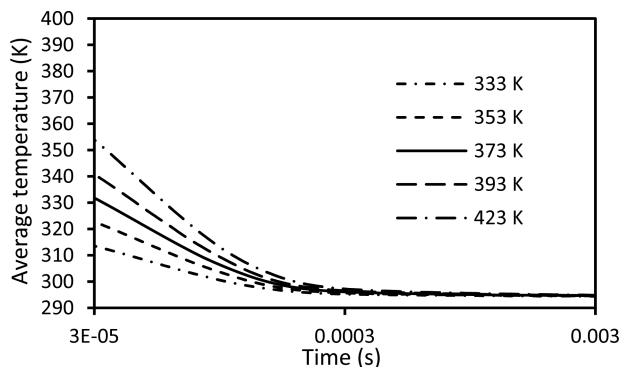


Figure 10. Semilog plot of the variation of the average bubble temperature at different initial bubble temperatures $T_0 = 423$ K (top line), 393, 373, 353, and 333 K (bottom line). The initial condition is bone dry air injected into the microbubbles.

1.6 mol/m^3 (Figure 9). The expected additional evaporation achieved by injecting higher bubble temperatures can be neglected at this level of heating because of two effects. First, the volumetric heat capacity of the liquid, which is the density of a substance multiplied by the heat capacity (ρC_p) is 3 orders of magnitude higher than that of the vapor.²² Second, the size of our computational domain is an order of magnitude larger than the bubble radius.

3.4. Variation of Liquid Mixture Concentration. In order to check the influence of ethanol content in the liquid phase on the heat and mass transfer dynamics of the bubble, a sensitivity study was performed which involved changing the mole fraction of ethanol in the liquid phase. Liquid properties such as density, viscosity, and surface tension have great impact on the bubble behavior as they can affect both the bubble size and the residence time.

Figure 11 shows the concentration profiles of ethanol at five different liquid ethanol mole fractions. The initial condition is bone dry air at an injection temperature of 393 K. Table 3 lists

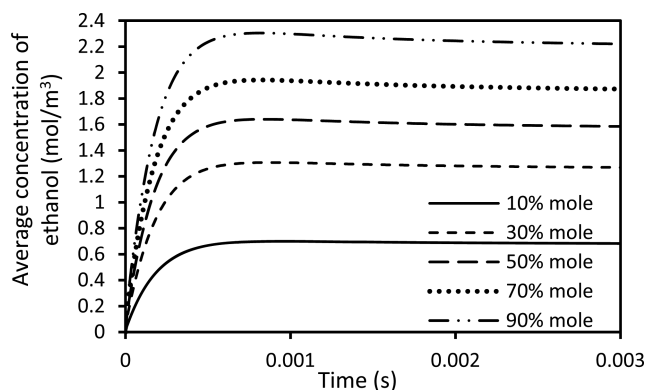


Figure 11. Average concentration profile data for ethanol at different liquid compositions: 90% mole ethanol (top line), 70% mole, 50% mole, 30% mole, 10% mole (bottom line). The initial condition corresponds to bone dry air at $T_0 = 393$ K injected into the microbubbles.

the concentrations of ethanol in the microbubble regime achieved by numerical calculations with the isothermal equilibrium values.⁴⁰

Not surprisingly, the average concentration of ethanol in the bubble phase increases as the concentration of ethanol in the ambient liquid phase rises as a result of increasing its proportion, and consequently its saturation pressure at the gas–liquid interface. The most interesting findings can be seen in the data presented in Table 3, which clearly demonstrate that the concentrations of ethanol in the bubble phase are higher than those achieved at equilibrium state within short residence times for all liquid ethanol compositions considered in this study. With sufficiently long contact times (in excess of around 0.003 s) the bubble achieves equilibrium conditions both chemically and thermally.

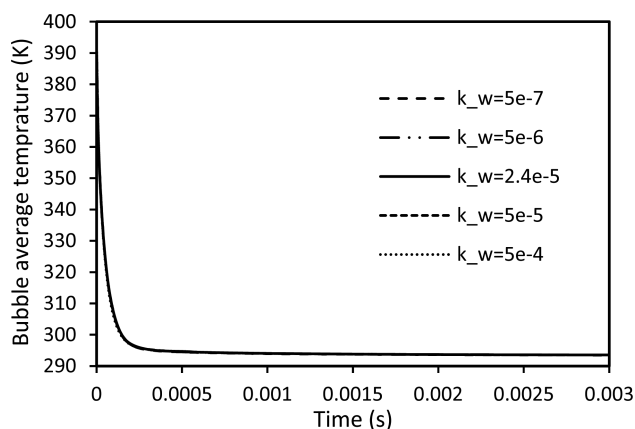
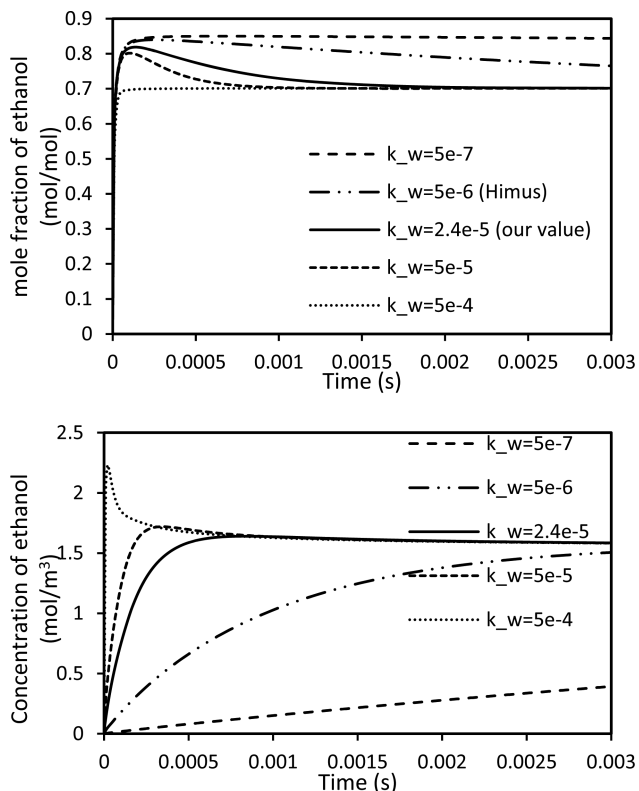
3.5. Variation of the Evaporation Parameter of Water (k_w). Although the value of the evaporation parameter of water (k_w) was estimated here by the least-squares analysis method using our experimental data from the separation of ethanol–water mixtures,²⁶ it is important to understand how this parameter affects the behavior of the system. Figures 12 and 13 show the sensitivity of the time profiles of the average temperature and concentration respectively to different values of k_w . The initial liquid ethanol concentration and the initial bubble temperature were fixed at 50% mole and 393 K for all cases.

It is clear from the data that the smaller is the value of k_w , the slower is the mass transfer evolution, and this is associated with nearly isothermal systems. On the other hand, large values of k_w (i.e., $k_w = 5 \times 10^{-4}$) correspond to flashing to equilibrium with rapid vaporization at very short contact time followed by recondensation as the bubble cools down once sensible heating has had time to act. It can also be noticed that the value applied in the current work (i.e., $k_w = 2.4 \times 10^{-5}$) ensures nonequilibrium dynamics that are appropriately rapid so it is consistent with the observation of our system which is neither always isothermal nor always at equilibrium.

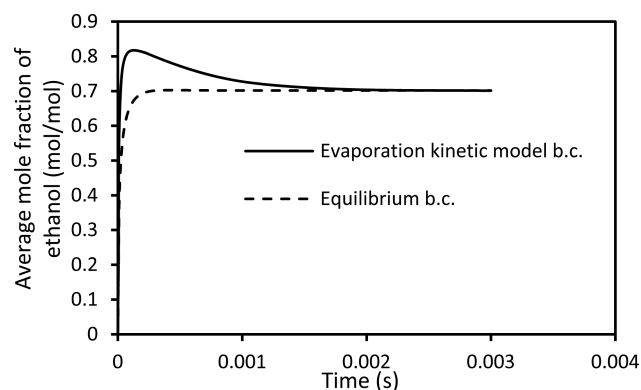
Figure 14 presents the difference between the mass boundary condition adopted here at the gas–liquid interface (i.e., eq 10) and that for the equilibrium state. The equilibrium boundary condition at the interface was stated by fixing the partial pressure of each component to the saturation pressure at the interface temperature (Raoult's law):

Table 3. Ethanol Vapor Concentrations in the Bubble Regime As Predicted by the Numerical Study and Isothermal Equilibrium Data for Different Initial Liquid Ethanol Mole Fractions

liquid concentration (% mol)	vapor concentration at $t = 0.00015$ s (% mol)	vapor concentration at $t = 0.003$ s (% mol)	final T_b at $t = 0.003$ s (K)	isothermal equilibrium data at final T_b (% mol)
10	59.9	43.6	293.4	44.9
30	75.8	62.0	293.5	60.9
50	81.9	70.1	293.5	68.6
70	87.3	78.2	293.6	77.6
90	94.6	90.2	293.5	90.8

**Figure 12.** Variation of the average temperature of the bubble with the evaporation parameter (k_w) of water. Initial bubble temperature is $T_0 = 393$ K and initial liquid concentration is 50% mole ethanol.**Figure 13.** Variation of the average concentration of ethanol with the evaporation parameter (k_w) of water, top is mole fraction (mol/mol) and bottom is concentration (mol/m³). The initial bubble temperature is $T_0 = 393$ K and the initial liquid concentration is 50% mole ethanol.

$$P_i = x_i \gamma_i P_i^* \quad (12)$$

**Figure 14.** Comparison between the average concentration profiles for ethanol for different boundary conditions at the gas–liquid interface.

To assess the validity of the model, the results of the vapor contents for a single microbubble have been compared with the results from our previous experimental work on the stripping of ethanol–water mixtures by hot dry air microbubbles.²⁶ The modeling approach adopted here used the concentration of this single bubble size to predict the concentration of ethanol that was measured experimentally at the top of the liquid mixture layer in the header space of the bubble tank.²⁶ Typically, the assumption of a single bubble size is reasonable for microbubbles generated by fluidic oscillation since interactions between bubbles are infrequent and bubble size distribution is very narrow.^{22,41,42}

The most challenging part in the comparison is computing the residence time of the bubbles in the liquid for our experiments. This time is a combination of three elements: (i) the formation time of the bubble from the pore of the diffuser, when it is in a contact with the liquid but has not been released, (ii) the ascending time in the liquid, and (iii) the time for the bubble to burst at the top surface. For this reason, we have taken the temperature of the header space as that measured by the experiments as an indication for the contact time at which the bubble exits. The average temperature in the header space for the range of liquid compositions that were tested in the experiments was around 300 K and according to the numerical results this value coincides with a residence time of about 0.00014 s, therefore this time has been used for the comparison.

The model predictions at $t = 0.00014$ s are compared with the experimental data in Figure 15. The same initial conditions were used in both the experimental work and the simulations for microbubble temperature, liquid mixture temperature, and liquid ethanol compositions.

It can be clearly seen that the experimental data are consistent with the predictions of the computational model at both the nonequilibrium stage (short residence times) and the

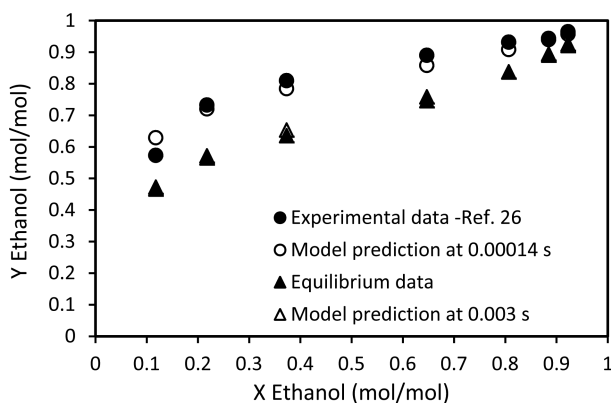
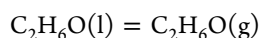


Figure 15. Comparison between experimental and modeling vapor mole fractions data (Y ethanol) for different liquid ethanol mole fractions (X ethanol) after 0.00014 and 0.003 s. The initial conditions are bone dry air with $T_0 = 363$ K injected into the microbubble and 293 K liquid temperature.

equilibrium stage (longer residence times) for all liquid ethanol compositions considered in the experimental work.

A plausible explanation for these results will now be considered. The injection of hot, bone dry air microbubbles into the cold liquid will give rise to nonequilibrium driving forces for the transfers of heat and mass between the contact phases. In the process described herein, microbubbles are injected into a laminar regime which acts so as to inhibit the liquid and gaseous phases from reaching equilibrium rapidly. This promotes the continuous transfer. In contrast to the situation for closed systems, in which liquid molecules can vaporize until equilibrium is established, the current configuration is analogous to an open system. Diffusion and internal convection arising from bubble motion lead to the continuous transfer of ethanol from the liquid side to the bubble side. Consequently, equilibrium is disrupted. According to Le Chatelier's principle the equilibrium position should be shifted toward increased vaporization to compensate for the molecules of ethanol that are removed by convection or diffusion:



In these circumstances the concentration of ethanol in the bubble phase is higher than the ratios found from equilibrium theory for all liquid phase mole fractions and within the short contact time available while the bubbles ascend in shallow liquid depths. The shallower the liquid depth is, that is, the shorter the contact time, the easier it is for nonequilibrium conditions to be maintained between the contacted phases, both chemically and thermally. This is crucial for continuing the transfer processes. In contrast, deeper liquid layers (longer contact times) are associated with a lesser quantity of vaporization since thermal equilibrium exists with the surrounding liquid. This effect is demonstrated in Table 3 which shows that as the residence time of the bubbles in the liquid is increased, the bubbles exiting the system are at equilibrium conditions.²⁶

4. CONCLUSIONS

A numerical study of a single superheated microbubble with internal circulation rising in a binary system of ethanol–water has been conducted. It was found that the enrichment of ethanol in the vapor phase is higher than the expected ratios of the equilibrium theory at short contact times for a range of

initial bubble temperatures and liquid ethanol compositions. It was also found that vaporization is faster than heat transfer to the liquid and that maximum evaporation occurs after a very short contact time. This leads to the conclusion that selectivity between evaporation and heat transfer can be engineered by controlling the residence time of the bubbles in the liquid so that maximum evaporation can be achieved with no or minimal heat transfer.

The simulation results were verified by comparing them with data obtained by previous experimental work on the separation of an ethanol–water system by hot air microbubbles.²⁶ The results from the single bubble model give an excellent prediction of the vapor concentrations obtained by the experimental work on thin liquid films at different liquid ethanol mole fractions.

AUTHOR INFORMATION

Corresponding Author

*E-mail: j.rees@sheffield.ac.uk.

Notes

The authors declare no competing financial interest.

ACKNOWLEDGMENTS

W.B.Z. thanks the EPSRC for support from the 4CU Programme Grant, 4cu.org.uk, (EP/K001329/1). W.B.Z. and J.M.R. thank Innovate UK and the EPSRC for a grant under the IB Catalyst industrial research scheme, EP/N011511/1. N.N.A. thanks the Higher Committee of Education and Development in Iraq for a doctoral scholarship.

REFERENCES

- (1) Dias, M. O. S.; Ensinas, A. V.; Nebra, S. A.; Maciel Filho, R.; Rossell, C. E. V.; Maciel, M. R. W. Production of bioethanol and other bio-based materials from sugarcane bagasse: Integration to conventional bioethanol production process. *Chem. Eng. Res. Des.* **2009**, *87*, 1206.
- (2) Quijada-Maldonado, E.; Aelmans, T. A. M.; Meindersma, G. W.; de Haan, A. B. Pilot plant validation of a rate-based extractive distillation model for water-ethanol separation with the ionic liquid [emim][DCA] as solvent. *Chem. Eng. J.* **2013**, *223*, 287.
- (3) Oliveira, F. S.; Pereiro, A. B.; Rebelo, L. P. N.; Marrucho, I. M. Deep eutectic solvents as extraction media for azeotropic mixtures. *Green Chem.* **2013**, *15*, 1326.
- (4) Pacheco-Basulto, J. A.; Hernandez-McConville, D.; Barroso-Munoz, F. O.; Hernandez, S.; Segovia-Hernandez, J. G.; Castro-Montoya, A. J.; Bonilla-Petriciolet, A. Purification of bioethanol using extractive batch distillation: Simulation and experimental studies. *Chem. Eng. Process.* **2012**, *61*, 30.
- (5) Onuki, S.; Koziel, J. A.; Jenks, W. S.; Cai, L.; Rice, S.; Leeuwen, J. H. V. Ethanol purification with ozonation, activated carbon adsorption, and gas stripping. *Sep. Purif. Technol.* **2015**, *151*, 165.
- (6) Julka, V.; Chiplunkar, M.; O'Young, L. Selecting Entrainers for Azeotropic Distillation. *Chem. Eng. Prog.* **2009**, *47*.
- (7) Corderi, S.; Gonzalez, B.; Calvar, N.; Gomez, E. Ionic liquids as solvents to separate the azeotropic mixture hexane/ethanol. *Fluid Phase Equilib.* **2013**, *337*, 11.
- (8) Francis, M. J.; Pashley, R. M. Application of a bubble column for evaporative cooling and a simple procedure for determining the latent heat of vaporization of aqueous salt solutions. *J. Phys. Chem. B* **2009**, *113*, 9311.
- (9) Ribeiro, C. P.; Lage, P. L. C. Direct-contact evaporation in the homogeneous and heterogeneous bubbling regimes. Part I: experimental analysis. *Int. J. Heat Mass Transfer* **2004**, *47*, 3825.
- (10) Ribeiro, C. P.; Lage, P. L. C. Gas-Liquid Direct-Contact Evaporation: A Review. *Chem. Eng. Technol.* **2005**, *28*, 1081.

- (11) Ribeiro, C. P.; Borges, C. P.; Lage, P. L. C. Modelling of direct-contact evaporation using a simultaneous heat and multicomponent mass-transfer model for superheated bubbles. *Chem. Eng. Sci.* **2005**, *60*, 1761.
- (12) Ribeiro, C. P.; Borges, C. P.; Lage, P. L. C. Sparger effects during the concentration of synthetic fruit juices by direct-contact evaporation. *J. Food Eng.* **2007**, *79*, 979.
- (13) Ribeiro, C. P.; Lage, P. L. C. Direct-contact evaporation in the homogeneous and heterogeneous bubbling regimes. Part II: dynamic simulation. *Int. J. Heat Mass Transfer* **2004**, *47*, 3841.
- (14) Jacobs, H. R. Direct-Contact heat transfer for process technologies. *J. Heat Transfer* **1988**, *110*, 1259.
- (15) Kang, Y. H.; Kim, N. J.; Hur, B. K.; Kim, C. B. A numerical study on heat transfer characteristics in a spray column direct contact heat exchanger. *KSME Int. J.* **2002**, *16*, 344.
- (16) Diaz, M. E.; Iranzo, A.; Cuadra, D.; Barbero, R.; Montes, F. J.; Galán, M. A. Numerical simulation of the gas-liquid flow in a laboratory scale bubble column. *Chem. Eng. J.* **2008**, *139*, 363.
- (17) Zimmerman, W. B.; Tesar, V.; Butler, S.; Bandulasena, H. C. H. Microbubble Generation. *Recent Pat. Eng.* **2008**, *2*, 1.
- (18) Zimmerman, W. B.; Hewakandamby, B. N.; Tesar, V.; Bandulasena, H. C. H.; Omotowa, O. A. On the design and simulation of an airlift loop bioreactor with microbubble generation by fluidic oscillation. *Food Bioprod. Process.* **2009**, *87*, 215.
- (19) Zimmerman, W. B.; Tesar, V.; Bandulasena, H. C. H. Towards energy efficient nanobubble generation with fluidic oscillation. *Curr. Opin. Colloid Interface Sci.* **2011**, *16*, 350.
- (20) Bredwell, M. D.; Worden, R. M. Mass-transfer properties of microbubbles. 1. Experimental studies. *Biotechnol. Prog.* **1998**, *14*, 31.
- (21) Worden, R. M.; Bredwell, M. D. Mass-Transfer Properties of Microbubbles. 2. Analysis Using a Dynamic Model. *Biotechnol. Prog.* **1998**, *14*, 39.
- (22) Zimmerman, W. B.; Al-Mashhadani, M. K. H.; Bandulasena, H. C. H. Evaporation dynamics of microbubbles. *Chem. Eng. Sci.* **2013**, *101*, 865.
- (23) Tesar, V.; Hung, C. H.; Zimmerman, W. B. No-moving-part hybrid-synthetic jet actuator. *Sens. Actuators, A* **2006**, *125*, 159.
- (24) Tesar, V. Paradox of flow reversal caused by protective wall-jet in a pipe. *Chem. Eng. J.* **2007**, *128*, 141.
- (25) Tesar, V.; Bandulasena, H. C. H. Bistable diverter valve in microfluidics. *Exp. Fluids* **2011**, *50*, 1225.
- (26) Abdulrazzaq, N.; Al-Sabbagh, B.; Rees, J. M.; Zimmerman, W. B. Separation of azeotropic mixtures using air microbubbles generated by fluidic oscillation. *AIChE J.* **2016**, *62*, 1192.
- (27) Yu, Z.; Fan, L. S. Direct simulation of the buoyant rise of bubbles in infinite liquid using level set method. *Can. J. Chem. Eng.* **2008**, *86*, 267.
- (28) Assael, M. J.; Trusler, J. P. M.; Tsolakis, T. F. *Thermophysical properties of fluids*; Imperial College Press: London, 1996.
- (29) Khattab, I. S.; Bandarkar, F.; Fakhree, M. A. A.; Jouyban, A. Density, viscosity, and surface tension of water+ethanol mixtures from 293 to 323K. *Korean J. Chem. Eng.* **2012**, *29*, 812.
- (30) Hill, M. J. M. On a Spherical Vortex. *Proc. R. Soc. London* **1894**, *55*, 219.
- (31) Panton, R. L. *Incompressible Flow*; John Wiley & Sons: New York, 1984.
- (32) Lamb, H. *Hydrodynamics*, 6th ed. (printed 1994); Cambridge University Press, 1879.
- (33) Campos, F.; Lage, P. L. Heat and mass transfer modeling during the formation and ascension of superheated bubbles. *Int. J. Heat Mass Transfer* **2000**, *43*, 2883.
- (34) Cui, X.; Li, X.; Sui, H.; Li, H. Computational fluid dynamics simulations of direct contact heat and mass transfer of a multi-component two-phase film flow in an inclined channel at sub-atmospheric pressure. *Int. J. Heat Mass Transfer* **2012**, *55*, 5808.
- (35) MacInnes, J. M.; Pitt, M. J.; Priestman, G. H.; Allen, R. W. K. Analysis of two-phase contacting in a rotating spiral channel. *Chem. Eng. Sci.* **2012**, *69*, 304.
- (36) Rivier, C. A.; García-Payo, M. C.; Marison, I. W.; Von Stockar, U. Separation of binary mixtures by thermostatic sweeping gas membrane distillation - I. Theory and simulations. *J. Membr. Sci.* **2002**, *201*, 1.
- (37) Himus, G. W.; Hinchley, A. R. S. M. The effect of a current of air on the rate of evaporation of water below the boiling point. *J. Soc. Chem. Ind., London* **1924**, *43*, 840.
- (38) Ubal, S.; Harrison, C. H.; Grassia, P.; Korchinsky, W. J. Numerical simulation of mass transfer in circulating drops. *Chem. Eng. Sci.* **2010**, *65*, 2934.
- (39) Ubal, S.; Grassia, P.; Harrison, C. H.; Korchinsky, W. J. Numerical simulation of multi-component mass transfer in rigid or circulating drops: Multi-component effects even in the presence of weak coupling. *Colloids Surf, A* **2011**, *380*, 6.
- (40) Mellan, I.; Flick, E. W. *Industrial Solvents Handbook*, revised 6th ed.; Noyes Publications, 1998.
- (41) Hanotu, J.; Bandulasena, H. C. H.; Chiu, T. Y.; Zimmerman, W. B. Oil emulsion separation with fluidic oscillator generated microbubbles. *Int. J. Multiphase Flow* **2013**, *56*, 119.
- (42) Hanotu, J.; Bandulasena, H. C. H.; Zimmerman, W. B. Microflotation performance for algal separation. *Biotechnol. Bioeng.* **2012**, *109*, 1663.